Response surface methodology approach for optimization of biosorption process for removal of Hg(II) ions by immobilized Algal biomass Coelastrella sp.

Ali Hussine AlSarji[1], Shurooq Talib Al-Humairi[1*], Riyadh Sadeq AlMukhtar[1], Saja Mohsen Alardhi[2], Mohamed Sulyman[3], I.M.R. Fattah[4]

[1]Chemical engineering department, University of Technology – Iraq, Baghdad 10066, Iraq
[2]Nanotechnology and Advanced Materials Research Centre, University of Technology- Iraq, Baghdad 10066, Iraq
[3]Department of Engineering and Environmental Sciences – The Libyan Academy-Misrata, Libya
[4]School of Civil and Environmental Engineering, Faculty of Engineering and IT, University of Technology Sydney, Ultimo, NSW, 2007, Australia
*Corresponding author: e-mail: shurooq.t.ramadhan@uotechnology.edu.iq

Currently, adsorption stands as a viable technique for the effective removal of pollutants such as heavy metals from water. Within this research endeavor, adapted green algae (*Coelastrella sp.*) have been harnessed as a sustainable and environmentally conscious adsorbent, employed in the removal of Hg(II) ions from a simulated aqueous solution via employment of an Airlift bioreactor. The analysis of the attributes of adsorbent was conducted through the utilization of Fourier transform infrared (FTIR) spectroscopy. The examination of residual concentrations of Hg(II) ions in the treated solution was accomplished through the utilization of atomic absorption spectroscopy (AAS). The impact of various experimental factors, including the duration of contact (ranging from 10 to 90 minutes), initial concentrations of Hg(II) ions (ranging from 500 to 2000 μg/l), quantity of adsorbent introduced (ranging from 0.1 to 0.7 g per 250 ml), temperature variations (ranging from 20 to 40 $^{\circ}$C), and airflow velocity (ranging from 200 to 300 ml/min), was systematically examined. For the optimization of adsorption efficiency, MINITAB 18 software was employed. The equilibrium data was subjected to analysis using the Langmuir, Freundlich, and Temkin isotherm models. Employing the framework recommended by MINITAB 18, the optimal parameters for adsorption were identified as 2000 μg/l for initial concentration, 90 minutes for contact time, 40 $^{\circ}$C for temperature, and 300 ml/min for airflow rate. The Langmuir equation yielded the highest adsorption capacity, measuring 750 μg/g at a temperature of 40 $^{\circ}$C.

Keywords: Adsorption; green algae; equilibrium; airlift bioreactor; kinetics.

INTRODUCTION

The removal of hazardous heavy metals from wastewater has grown to be a significant global issue. Effluents resulting from many industries, including pulp and wood industries, paper board mills, metal cleaning and plating, and municipal wastewater, are the primary causes of heavy metal contamination[1–5]. Mercury, Hg (II), and its derivatives are cumulative poisons detrimental to human health, even at a very low concentration[6–8]. The discharge of effluents containing mercury into the ecosystem has the potential to pose threats to aquatic organisms and exert significant ramifications on the ecological food web. The pronounced toxicity associated with this element, its propensity to accumulate within soil and sediment matrices, and a series of notable ecological events, particularly exemplified by the Minamata Bay incident in Japan between 1953 and 1956, collectively catalyzed the advancement of methodologies aimed at the mitigation of mercury-laden effluents[9]. Currently, coal-fired power stations represent the most substantial contributor to atmospheric emissions. Nevertheless, the widespread utilization of mercury in dental amalgam implies that crematoria could potentially surpass them as the most significant source in the future. Additionally, hospitals equipped with medical waste incinerators play a significant role in contributing to the mercury issue. Although the number of medical waste incinerators is decreasing, resulting in reduced emissions, concerns persist within the healthcare community regarding the exposure of patients and other vulnerable groups to mercury through

the use of healthcare products. Furthermore, the chlor-alkali industry, being the largest consumer of mercury in Europe, has discharged numerous tons of mercury into the aquatic environment over the years, thereby contributing to fish contamination[10]. Mercury contamination may occur from a variety of sources, including effluents from chlorine manufacture, switchgear/batteries, fluorescent lights, dental wastes, paints, fertilizers, and medicines. Several of conventional technologies such as chemical precipitation, traditional coagulation, activated carbon adsorption, lime softening, ion exchange, and reverse osmosis have been used to remove mercury from contaminated water[11]. Because of the high cost of commercial activated carbon, there has been a quest for acceptable low-cost adsorbents. Due to its low cost, great effectiveness, minimal secondary waste, and environmental friendliness, biosorption has been widely used method in treating polluted water to reduce hazardous contaminants like mercury present in industrial effluents. Coelastrella is a genus of green algae in the family Scenedesmaceae. Coelastrella species may be found in a variety of terrestrial settings, including soil, tree bark, rock surfaces, concrete floors, and brick walls. Tolerance to a very broad temperature range allows for an overall distribution that spans the tropical and polar zones[12]. Green algae has been used as a renewable adsorbent to minimize chemical consumption in the waste treatment process, lowering the cost of the treatment plant indirectly[13]. The primary objective of the present study is to examine the effectiveness of eliminating mercury (II)

ions from a water-based solution utilizing green algae (Coelastrella sp.) within an Airlift Bioreactor setup. To optimize the impact of diverse variables, a full factorial design was employed. Adsorption isotherm models such as (Langmuir Isotherm, Freundlich Isotherm, and Temkin Isotherm), Thermodynamic study, Kinetic studies such as (Pseudo first-order, Pseudo second-order), and Mass transfer adsorption models such as (Weber and Morris model, Liquid film diffusion model, and Bangham and Burt model) are employed to assess the performance of the adsorbents and optimize their efficiency.

MATERIALS AND METHODS

Stock solution preparation

Mercury chloride $HgCl_2$ was obtained commercially from (Merk), (CAS #: 7487-94-7), (EC Number: 231-299-8). It has the molecular formula $HgCl_2$. The stock solution with a concentration of 1000 mg/l was meticulously formulated by completely dissolving the precisely measured amount of $HgCl_2$ (1.3520 g) in distilled water. Subsequently, various solutions of distinct concentrations were derived from this original solution through dilution, resulting in the desired concentrations (2000 μg/l, 1000 μg/l, 750 μg/l, and 500 μg/l).

Preparation of the biomass

For approximately a century, the genus Coelastrella has been acknowledged and encompasses a limited array of species. Coelastrella species exhibit a coccoid morphology, ranging from elliptical to citriform. These microorganisms can be observed as individual unicellular microalgae or as small clusters of cells. A distinctive feature of these species lies in their intricately textured cell walls, characterized by 16–40 meridional ribs and polar thickenings. The cellular envelope comprises two layers, featuring an internal cellulose constituent and an exterior trilaminar component housing an acetolysis-resistant material[14].

First and foremost, the initial step involves the preparation of the algae culture medium by utilizing NPK 20:20:20 (Table 1) as the nutrient medium. As per the research conducted by[15], a concentration of 1g/L of NPK medium was employed to facilitate the growth of green algae. The assessment of the costs associated with cultivating the media was carried out by exclusively considering the concentration and price of each reagent employed in the production of 1 L of the medium. Subsequently, the medium underwent a process of sterilization through indirect heating until it reached a temperature range of 45–50 ºC. Once the medium had sufficiently cooled to room temperature, the algae were introduced. The particular strain of algae was acquired from the department of biology at the College of Science, University of Baghdad. To be precise, a volume of 50 ml of algae, with a concentration of 14–16 x 106 cell/ml, was incorporated into five liters of water containing the nutrient medium. The photobioreactor employed in this study was a plastic bottle with a capacity of five liters. All the necessary requirements for the growth of algae were adequately provided. Notably, one of the crucial needs of algae is light, hence, three LED lights were affixed to each bottle. These LED lights, with a brightness of 1 k lux, were supplemented with 13-watt fluorescent bulbs to ensure the completion of the photosynthesis process. In addition to light, carbon dioxide is another essential requirement for the growth of algae. As such, carbon dioxide gas from the ambient air was effectively introduced into the bioreactor at a steady flow rate of 200 ml/min. Following a period of approximately three weeks, the algae had successfully proliferated and were subsequently harvested. The resulting biomass concentration ranged from 0.4 to 0.7 g/L.

After the cultivation process, the Algae can be converted biomass than grinding it. Extracting algae from its culture area is referred to as harvesting. The principle of separate solid-liquid processes underpins algae processing. One of the most important steps of harvesting is thickening the algae solution until it forms a thick algal slurry or cake. After that drying process take place. Finally, it was milled and sieved through a 200 mesh sieve before being employed as an adsorbent.

Table 1. Presents the composition of N:P:K

Element	Value (%)
N as CH_4N_2O	2%
N as NH_3	18%
P as phosphorus oxide	20%
K as potassium oxide	20%
Mg+Zn+Mn+Fe+Cu	>1%

Design of experiments

Response Surface Methodology was used to optimize the four independent variables like Time (A), Temperature (B), Concentration (C) and AFR (D) for the adsorption of Hg (II) on biomass. MINITAB 18 (Full factorial design) recommended experimental design for four variables with experimental and expected response in 120 runs. Where five levels of time (10, 30, 50, 70 and 90 min), temperature levels (20, 30 and 40 ºC), Concentration levels (500, 750, 1000 and 2000 μg/l), and AFR levels (200 and 300 ml/min).

Airlift reactor

The adsorption of methylene blue onto algae was in transparent perspex split-cylinder airlift reactor. The reactor was made up of a vertical cylindrical column with a diameter of 7 cm and a length of 40 cm , with baffle 35-cm length as shown in Figure (1). The temperature of the airlift reactor was measured using a temperature sensor situated at the reactor's top and kept at (20–40 ºC) using a heater. The air is directed through the first side in order to transform into the riser, which was accomplished by utilizing a 25W, 2 bar pressure air compressor. The distribution of the air was achieved through the utilization of a small air-permeable stone. The reactor is securely sealed in order to prevent any external air from infiltrating the internal space, and this was accomplished by implementing a one-way valve. Figure (1) illustrates a schematic diagram depicting the operational configuration of the experimental airlift reactor. The reactor work in semi-batch mode.

Adsorption experiments

Adsorption experiments were carried out in an airlift bioreactor under various operating conditions such as
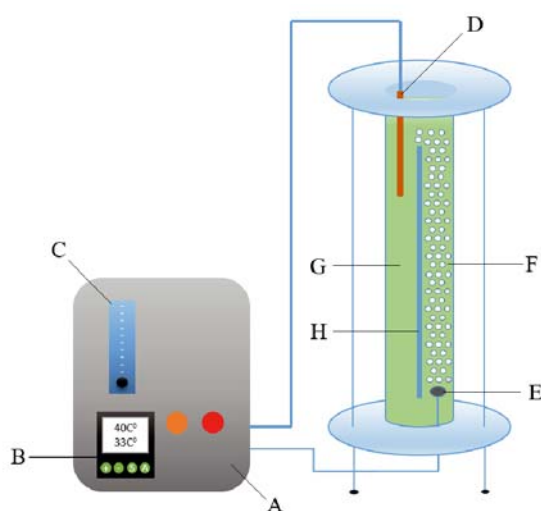
Figure 1. Schematic diagram of Airlift reactor (A – Compressor, B – Temperature controller, C – Rotameter, D – Heater, E – Sparger, F – Riser, G – Downcomer, H – split)

contact time (10–90 min), temperature (20–40 °C), air flow rate (200–300 ml/min), concentration (500–2000 μg/l), and adsorbent dose (0.1–0.7 g/250 ml). In order to optimize the adsorption conditions in the ensuing isotherm and kinetic experiments. Obtained data from the impacts of operating conditions were then used for isotherm, kinetic, and thermodynamic analyses, respectively. The remaining concentration of Hg (II) was assessed employing the atomic absorption spectrophotometer (AAS) Perkin Elmer 1100 model. The equilibrium's adsorption capacity (q_e, μg/g) and efficiency (R, %) were computed using Equation (1) and (2), respectively[16, 17].

$$q_e = (C_i - C_e)\frac{V}{W} \tag{1}$$

$$Removal\% = \frac{c_i - c_e}{c_i} \times 100 \tag{2}$$

where: C_i and C_e (μg/l) are the initial and final Hg (II) concentration, respectively. V is the volume of the solution (L), M is the amount of adsorbent (g).

RESULTS AND DISCUSSION

Characterization of the synthesized adsorbent

Fourier-transform Infrared Spectroscopy (FTIR) stands as a widely acknowledged method for characterizing both inherent and newly-formed functional groups resulting from chemical processes. In this investigation, an Shimadzu model 1800 instrument was employed, operating within a frequency range spanning from 400 to 4000 cm^{-1}, to acquire the IR spectra of the adsorbent before and after the adsorption procedure. The enumeration of all functional groups present on the surface of the algae biomass is detailed in Table 2. Figures 2 and 3 show the examination before and after the adsorption process.

Scanning electron microscopy (SEM)

Scanning electron microscopy (SEM) serves as an initial and essential instrument for assessing the surface morphology and fundamental physical attributes of adsorbents. The examination of sample surface morphology before and after the adsorption process was conducted through SEM analysis. SEM is particularly adept at evaluating the adsorption capacity of compounds, as the surface structure and porosity predominantly govern the
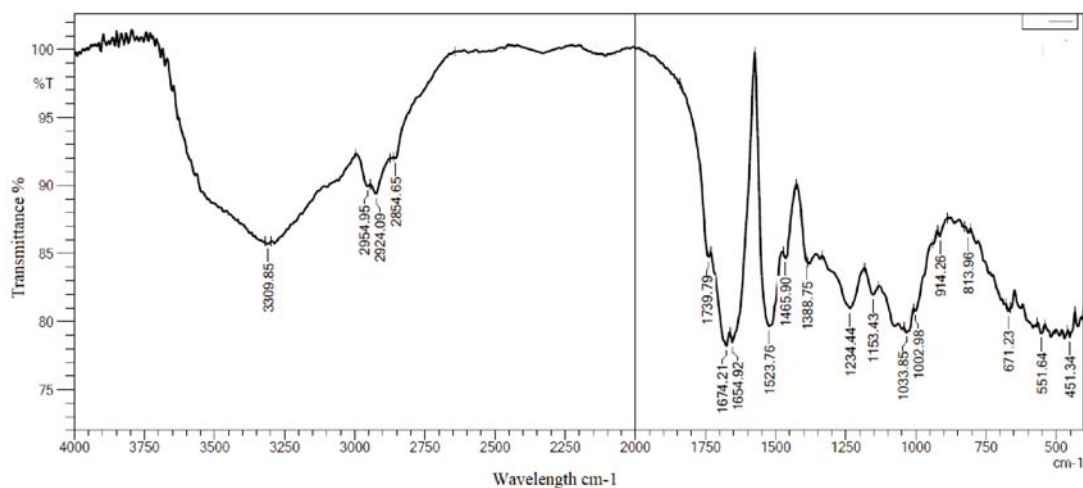

Figure 2. FTIR spectrum for algae before adsorption of mercury

Table 2. IR spectra of the adsorbent before and after adsorption process

| Wave number Before	Wave number After	Wave number Range	Vibration	Functional group present
3292.88	3274.84	3300–2500	O-H stretching	Alcohol, phenols, Carboxylic acid
2925.85	2924.84			
1638.35	1633.80	1650–1600	C=C stretching	Conjugated alkene
1535.43	1538.09	1550–1500	N-O stretching	Nitro compound
1451.52	1453.96	1450	C-H bending	Alkane
1387.26	1395.52	1420–1330	O-H bending	Alcohol
1232.28	1236.98	1275–1200	C-O stretching	Alkyl aryl ether
–	1151.46	1250–1020	C-N stretching	Amine
–	1076.73	1085–1050	C-O stretching	Primary alcohol
1039.20	1028.80	1250–1020	C-N stretching	Amine
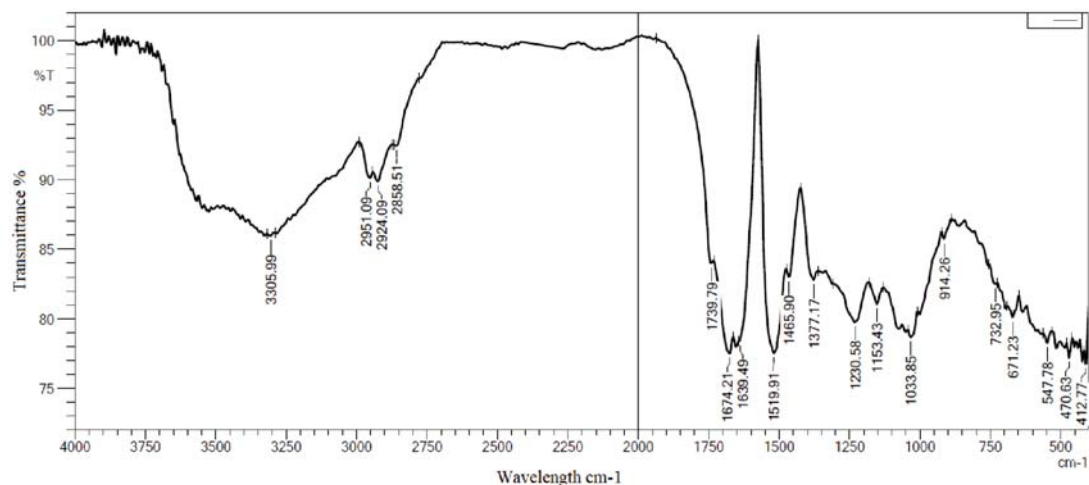
Figure 3. FTIR spectrum for algae after adsorption of mercury

adsorption capacity[18, 19]. Figure 4 depicts SEM images of algae before and after the adsorption process. In Figure 4-a, it is evident that the structural integrity of the algae cells persists post-drying. In contrast, Figure 4-b illustrates a distinct transformation wherein the cells have disintegrated, leading to a notable deviation from the original state. The previously porous surface has transitioned to a flakier morphology exhibiting residual porosity. Consequently, the SEM imagery provides supplementary substantiation regarding the adsorption of metal ions.

Energy Dispersive Spectroscopy (EDS)

Energy Dispersive Spectroscopy (EDS) were done using thermos fisher Scanning electron microscope. Figure 5 depicts the elemental surface composition of algae obtained. The presence of C and O atoms with some impurity was confirmed by the Figure 5-a. The presence of some impurities due to the algae medium. The pattern reveals that the algal sample's composition is C – 54.3%, O – 45.3%, with the remainder being contaminants. The EDS spectra of Hg doped algae is shown in figure 5-b. According to the EDS spectrum, the synthesized Hg doped algae biomass mostly contains C, O, and Hg elements, with a composition of C – 56.2%, O – 37.8%, and Hg – 2.8%.

Statistical analysis

Response surface methodology amalgamates statistical and mathematical approaches, finding extensive utilization in optimizing variables across various applications[20].
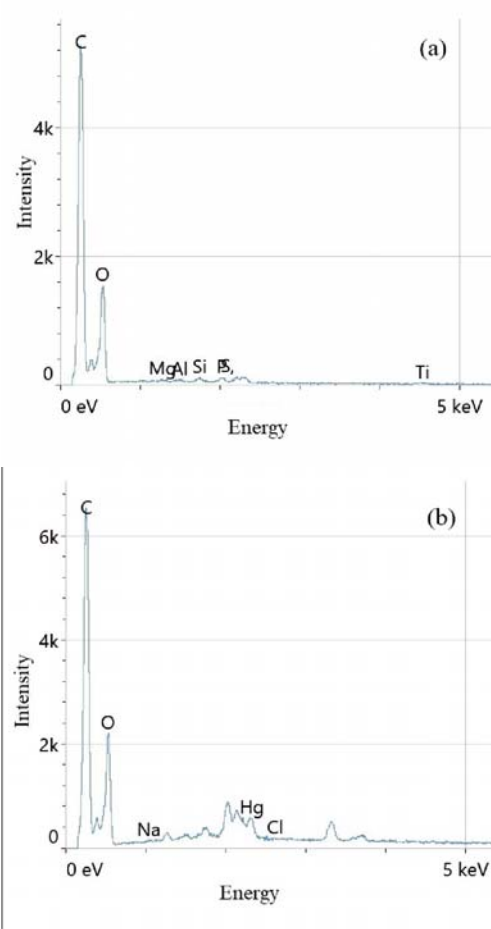

Figure 5. Energy dispersive spectroscopy before adsorption (a), and after adsorption (b) of mercury by algae
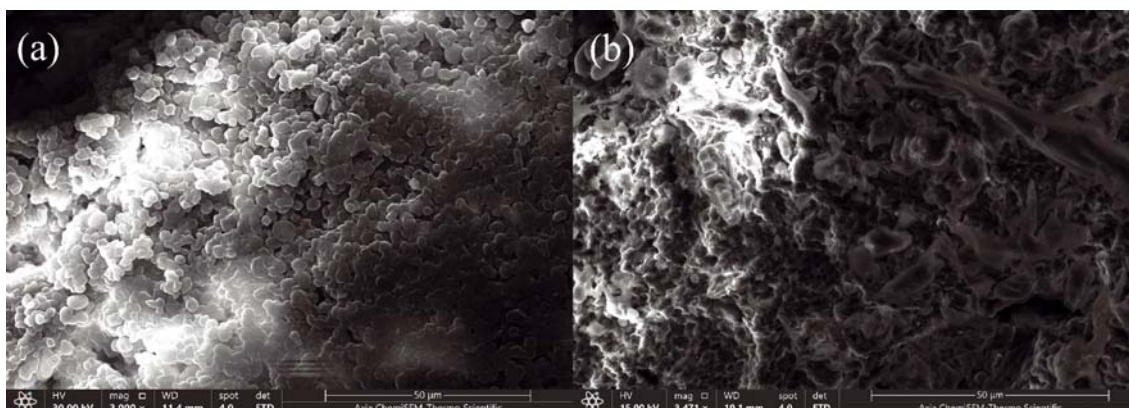

Figure 4. SEM images of algae before (a), and after (b) adsorption process of mercury

Utilizing MINITAB 18, a comprehensive investigation comprising 120 tests was recommended to scrutinize the interplay of four variables: time (A), temperature (B), concentration (C), and AFR (D). Based on the collected experimental data, establishing a relationship between the response and the encoded values of the four variables. This process yielded an empirical equation, as detailed below:

$$Removal\% = 65.7 + 0.3937\,A + 0.531\,B - 0.02085\,C +$$
$$+ 0.0213\,D - 0.00900\,AB + 0.000110\,AC - 0.000042\,AD +$$
$$+ 0.000343\,BC - 0.000150\,BD - 0.000003\,CD \quad (3)$$

In Equation 3, the positive sign implies a synergistic impact, whereas the negative sign indicates an antagonistic effect behavior[21]. A higher F value and a lower P value indicated the significance of each coefficient[22].

Analysis of variance

The statistical significance and appropriateness of the regression model constructed through full factorial design were assessed using Analysis of Variance (ANOVA), the results of which are presented in Table 3. Fisher's F values and P values were employed in conjunction with the null hypothesis test to determine the significance of both the regression model and each individual coefficient term[23]. Generally, higher F values coupled with lower P values indicate enhanced significance of the regression model and associated coefficients[24]. As indicated in Table 3, the full factorial design model exhibits pronounced significance, evident from a substantial F value of 47.44 and an impressively low P value of 0.00. Similarly, other specific coefficients such as linear and 2-Way Interactions also demonstrate remarkable significance, with F values of 111.04 and 10.64, respectively, and P values lower than 0.01. Subsequently, components lacking statistical significance (p > 0.05) are eliminated from the quadratic equation. This process results in the formulation of an adjusted factorial design model, achieved through consideration of the T and P values presented in Table 3.

$$Removal\% = 65.7 + 0.3937\,A + 0.531\,B - \quad (4)$$
$$- 0.02085\,C - 0.00900\,AB + 0.000110\,AC + 0.000343\,BC$$

The model's adequacy was determined by the correlation coefficients R^2 and R^2_{adj}. The values of R^2 and R^2_{adj} were determined to be 0.90 and 0.88, respectively, based on the ANNOVA findings.

Three dimensional response surface plot and contour plots

Three-dimensional surface plots serve as visual depictions of regression equations, illustrating the simultaneous effect of two variables on a response while maintaining the constancy of the remaining variable[25]. Alternatively, two-dimensional contour plots can be employed to explore the influence of any two factors through two-dimensional graphical representations. In Figures 6, 7, and 8, both 3D surface plots and their corresponding 2D contour plots are displayed, elucidating the interactive influence of individual variables on the percentage removal of Hg (II).
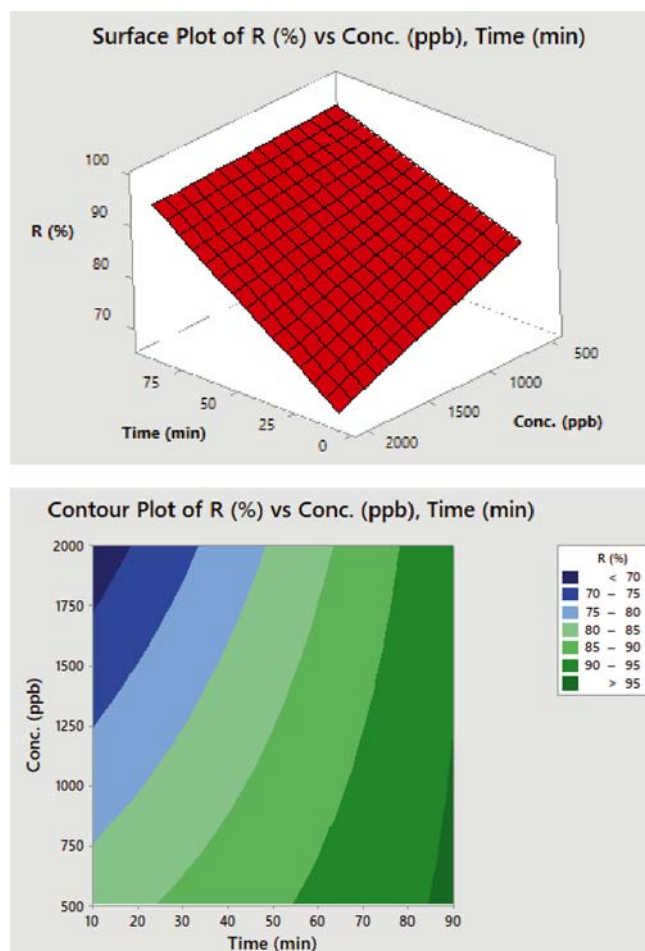

Figure 6. 3D surface plot for interactive effect of time and concentration on Removal of Hg(II) (a), 2D contour plot for interactive effect of time and concentration on Removal of Hg(II) (b)

Table 3. Present the Variance Analysis

Source	DF	Adj SS	Adj MS	F-Value	P-Value
Model	10	8922.7	892.27	47.44	0.000
Linear	4	8353.7	2088.43	111.04	0.000
Time (min)	1	5439.2	5439.16	289.19	0.000
Temp. (C)	1	1606.2	1606.20	85.40	0.000
Cons. (ppb)	1	1272.4	1272.45	67.65	0.000
AFR (ml/min)	1	35.9	35.91	1.91	0.170
2-Way Interactions	6	1200.2	200.04	10.64	0.000
Time (min)*Temp. (C)	1	518.4	518.40	27.56	0.000
Time (min)*Cons. (ppb)	1	375.8	375.79	19.98	0.000
Time (min)*AFR (ml/min)	1	0.4	0.42	0.02	0.882
Temp. (C)*Cons. (ppb)	1	304.5	304.53	16.19	0.000
Temp. (C)*AFR (ml/min)	1	0.4	0.45	0.02	0.877
Cons. (ppb)*AFR (ml/min)	1	0.6	0.64	0.03	0.854
Error	109	1096.2	18.81		
Total	119	10972.8			

In Figure 6, both panel (a) and (b) present the 3D surface plot and the corresponding contour plot, respectively, illustrating the interdependent effect of time and concentration on the eradication of Hg(II). It is evident from the visualization that an increase in concentration from 500 ppb to 2000 ppb leads to a decline in the percentage of Hg(II) ion removal over time. This decline can be attributed to the saturation of adsorbent sites with Hg(II) ions at a constrained concentration[26]. Meanwhile, in Figures 7 (a & b), a discernible enhancement in the percentage removal of Hg(II) ions is showcased in tandem with an escalation in temperature, ranging from 20 to 40 °C, and a lengthening of time, spanning 10 to 90 minutes. Notably, the advancement in the percentage of Hg(II) ion removal remains modest, progressing from 91% to 97%. This trend can be elucidated by the heightened mobility of dye molecules as the temperature rises, indicating the involvement of a kinetic regulatory mechanism—a phenomenon consistently observed across various systems[27]. Figures 8 (a) and (b) depict the 3D surface plot and its corresponding contour plot, illustrating the interplay between AFR and time regarding the reduction percentage of Hg(II) ions, while keeping the concentration constant at 750 ppb and the temperature at 30 °C. As can be observed, increasing AFR from 200 ml/min to 300 ml/min with time enhances the removal % for Hg(II) ions just marginally. This means that the effect of air flow is not directly affecting on adsorptions process.
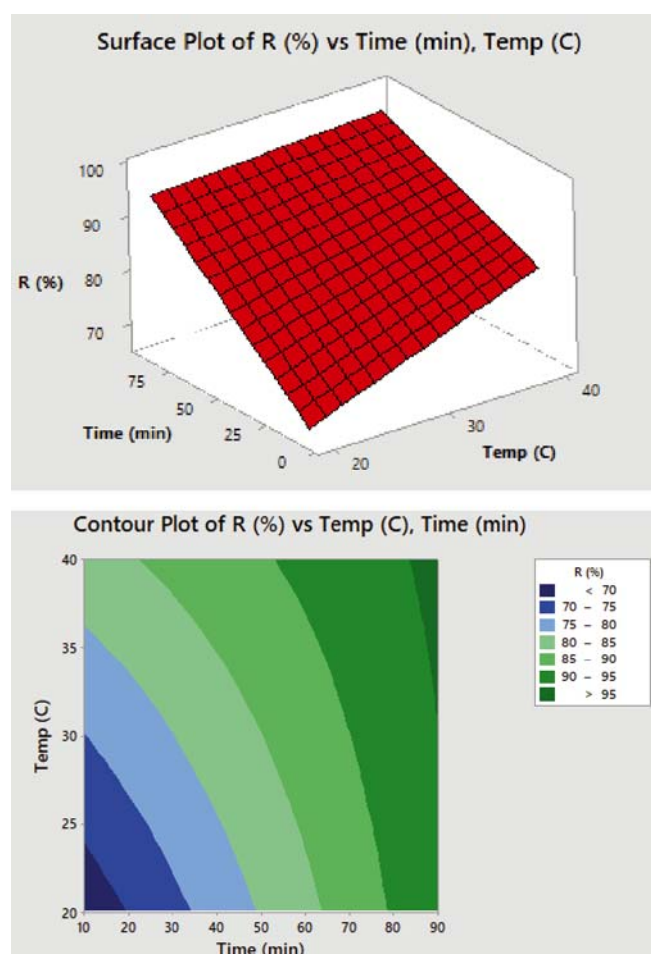

Figure 7. 3D surface plot for interactive effect of time and temperature on Removal of Hg(II) (a), 2D contour plot for interactive effect of time and temperature on Removal of Hg(II) (b)
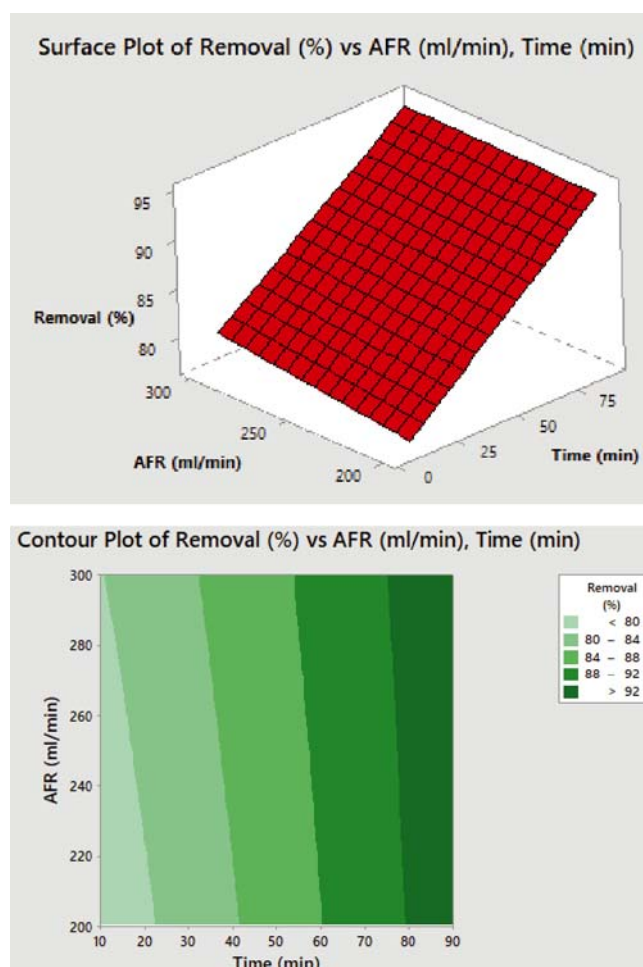

Figure 8. 3D surface plot for interactive effect of time and concentration on Removal of Hg(II) (a), 2D contour plot for interactive effect of time and concentration on Removal of Hg(II) (b)

The effect of adsorbent dose

The effect of varying the adsorbent dosage on the adsorption of mercury ions and are shown in Figures (9) One of the most important variables influencing the biosorption process is the biomass dose, which is used to calculate the biosorbent capacity for a given initially concentration[28]. Various amounts of algal biomass (0.1–0.7 g/250 ml) have been used in this study. It is clearly seen that the removal efficiency of Hg(II) ions increases from 30.8% to 95.7% as the algae biomass increases from 0.1 to 0.5 g/250 ml at concentration 1000 ppb and temperature 40 °C. because of a screen effect between biomass, the adsorption capacity remained constant, resulting in a block of the biomass functional groups[29] or because it is known that high doses of biomass produce agglomeration, which in turn decreases the intercellular distance and hence protects binding sites from contaminant exposure[30]. Increases in biomass concentration often result in increased solute biosorption because more binding sites are available per unit of biosorbent surface area[31]. Because all sites were completely exposed to the pollutant at low biomass doses, the surfaces were saturated quicker, resulting in a larger value of q_e. Nonetheless, when the proportion of lower energy sites occupied grew with increasing doses of biomass, the availability of higher energy dropped, resulting in a lower qe value.
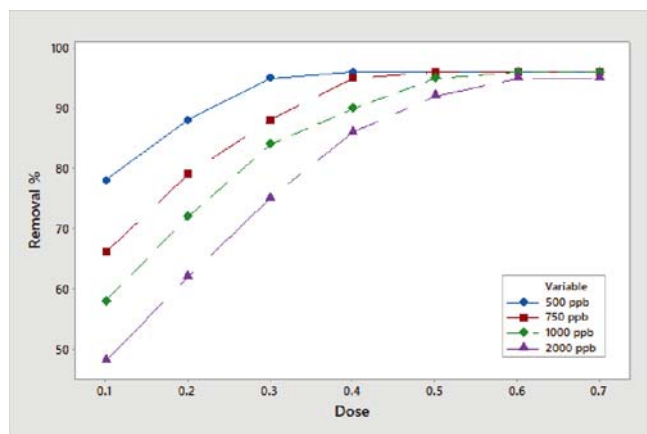
Figure 9. Effect of adsorbent dose on the rate of adsorption

Adsorption isotherms

Adsorption isotherm models were used to improve predictions of the connection between target species concentration and adsorbent surface[32]. To correlate the adsorption process of Hg(II) on algae, the equilibrium data was applied to three well-known adsorption models. The linear form of the isotherm models including, Langmuir[33], Freundlich[34], and Temkin[35] are given by Equation 6, 7, and 8, respectively.

Langmuir Isotherm

The Langmuir adsorption isotherm investigation involved the systematic alteration of the initial concentration of Hg(II) ranging from 500 μg/l to 2000 μg/l , while maintaining all other parameters constant. The linear representation of the Langmuir adsorption is conveyed by Equation (5)[25]. The Langmuir parameters were deduced from the gradient and intercept of the linear regression line established for the uptake of Hg(II) ions using green algae, as depicted in Figure 10 and summarized in Table 4. The congruence of the green algae adsorption data with the Langmuir model signifies the uniform nature of the adsorbent surface in relation to the binding of metal ions. Additionally, the high coefficient of determination (R^2) value of 0.9981 underscores a strong correspondence between the Langmuir constants and validates the assertion of monolayer adsorption of metal ions onto the adsorbent surface. Algae biomass was found to have a maximum adsorption capability of 495 g/g.

$$\frac{C_e}{q_e} = \frac{1}{q_{max}K_L} + \frac{C_e}{q_{max}} \tag{5}$$

where:
C_e is the equilibrium concentration of adsorbate (μg/g).
q_e is adsorption capacity at equilibrium (μg/g).

q_{max} is the maximum adsorption capacity (μg/g).
K_L is the Langmuir isotherm constant (L/mg).

The separation factor RL, also recognized as the equilibrium parameter, is a dimensionless constant employed to encapsulate the fundamental attributes of the Langmuir isotherm[29].

$$R_L = 1 / (1 + K_L Ci) \tag{6}$$

Where: C_i is the initial concentration, K_L is the Langmuir isotherm constant (L/mg), R_L value indicates the adsorption nature to be either unfavorable if $R_L > 1$, linear if $R_L = 1$, favorable if $0 < R_L < 1$ and an irreversible if $R_L = 0$.

Freundlich Isotherm

The Freundlich parameters were calculated using the slopes and intercepts of the linear plots for Hg(II) ions uptake using green algae, as shown in Figure (11) and Table (4). The adsorption capacity and intensity were represented by the Freundlich constants K_f and n, respectively. The linear form of the Freundlich isotherm model is given by Equation (7)[27].

$$\log q_e = \log K_f + \frac{1}{n}\log C_e \tag{7}$$

Where: q_e = the amount of metal adsorbed per gram of the adsorbent at equilibrium (μg/g).
K_f = an approximate indicator of adsorption capacity.
1/n = a function of the strength of adsorption in the adsorption process.
C_e = the equilibrium concentration of adsorbate (μg/l)[36].

Temkin Isotherm

$$q_e = B \ln A_T + B \ln C_e \tag{8}$$

q_e = the amount of metal adsorbed per gram of the adsorbent at equilibrium (μg/g).
A_T = Temkin isotherm equilibrium binding constant (L/g).
B = Constant related to heat of sorption(J/mol)[36].

The selection of a suitable model is determined by the presence of a high regression coefficient R^2[37]. The derived parameters and the linearly fitted graph depicting the Temkin adsorption isotherm model are furnished in Table 4 and Figure 12. It is important to highlight that the configuration of the adsorption isotherm can provide substantial insights into the underlying adsorption mechanism. Collectively, as demonstrated, the Langmuir model offers a superior elucidation of the Hg(II) adsorption on algae, exhibiting a more substantial R^2 value compared to both the Freundlich and Temkin models. The Langmuir model's linear fitting yielded a maximum monolayer adsorption capacity of 750 μg/g at 40 ^{o}C and

Table 4. Isotherm parameters

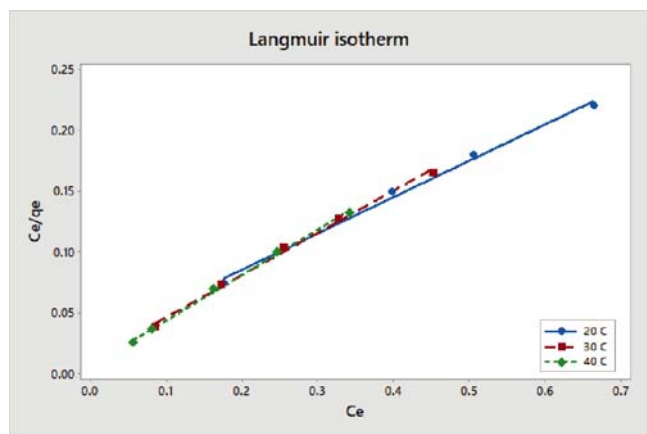| Type of isotherm	Parameters	20 C	30 C	40 C
Langmuir	Q_0 (μg/g)	432	474	495
	b (L/mg)	39.73	87.06	167.83
	R^2	0.9951	0.9961	0.9981
	R_L	0.0324	0.015	0.00788
Freundlich	K_F	0.243	0.296	0.325
	N	4.58	7.77	10.78
	R^2	0.9676	0.9374	0.9473
Temkin	A	0.0758	0.0048	0.000325
	B	−0.0825	−0.0523	−0.039
	R^2	0.9785	0.9513	0.9564

Figure 10. Langmuir isotherm plot for the adsorption of Hg(II) onto algae biomass
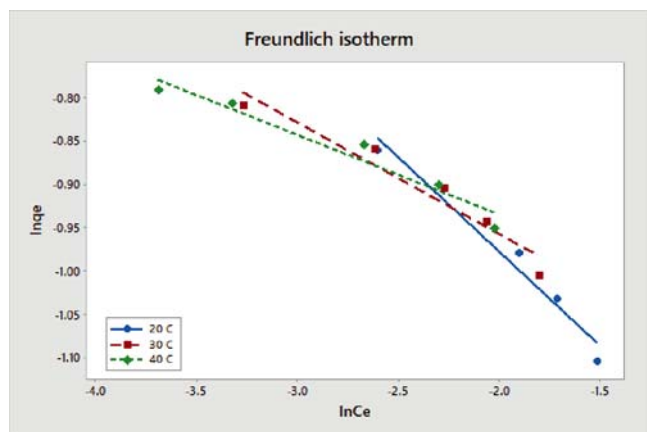

Figure 11. Freundlich isotherm plot for the adsorption of Hg(II) onto algae biomass
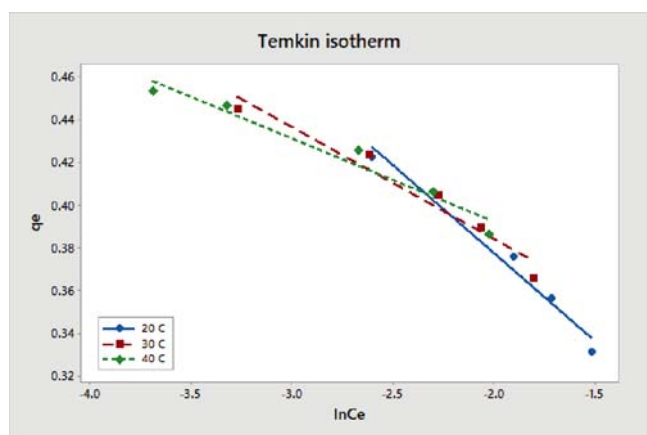

Figure 12. Temkin isotherm plot for the adsorption of Hg(II) onto algae

an initial concentration of 2000 ppb, signifying the favorable nature of the adsorption phenomenon.

Thermodynamic study

Thermodynamic parameters were manipulated within the temperature range of 20–40 °C, while maintaining initial Hg(II) ion concentrations at 750 ppb, and optimizing AFR and dose conditions. The thermodynamic attributes characterizing the absorption of Hg(II) ions by the algae biomass are organized in Table 5. Enthalpy and entropy values were extracted from the inclination and y-intercept of the ln Kc against 1/T graph, depicted in Figure 13. The obtained ΔH° value (40.62 kJ/mol) indicates an endothermic nature of the adsorption pro-

cess. The negative ΔG° values (–4.893 to –8.011kJ/mol), signify the spontaneous nature of bioadsorption. The positive ΔS° value (154.86 J/mol K) implies heightened disorderliness at the solid/liquid interface during the bioadsorption of Hg(II) onto the algae biomass.

$$K_C = \frac{q_e}{C_e} \tag{9}$$

$$\Delta G^o = -RT \ln K_C \tag{10}$$

$$\ln K_C = \left(\frac{\Delta S^o}{R}\right) - \left(\frac{\Delta H^o}{RT}\right) \tag{11}$$

Where: K_C is the represents equilibrium constant of the adsorption, T is the temperature in K, and R is the gas constant.

Table 5. Thermodynamic parameters for the removal of Hg(II) by algae biomass

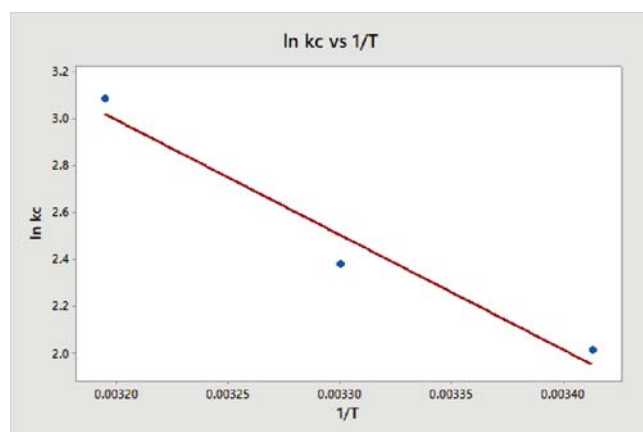| T (K)	ΔG^0 (kj/mol)	ΔH^0 (kj/mol)	ΔS^0 (j/mol)
293.15	–4.893		
303.15	–5.981	40.62	154.86
313.15	–8.011		

Figure 13. Van't Hoff plot for the removal of Hg(II) by algae bioadsorbent

Kinetic studies

The pseudo first and second-order kinetic models were used to explore the adsorption process of Hg(II) ions on the surface of algae with initial metal concentrations ranging from 500 to 2000 ppb.

Pseudo first-order

$$log(q_e - q_t) = log\, q_e - K_1 \frac{t}{2.303} \tag{12}$$

Where K_1 = the rate constant of adsorption
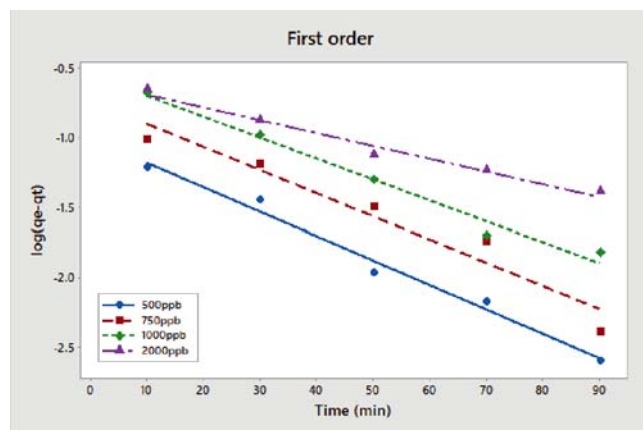

Figure 14. Pseudo-first-order kinetic model

Pseudo second-order

$$\frac{t}{q_t} = \frac{1}{K_2\, q_e{}^2} + \frac{t}{q_e} \qquad (13)$$

Where K_2= the rate constant of pseudo-second-order kinetic model.

Understanding the adsorption mechanism and the potential controlling steps in terms of rate is essential for designing effective waste effluent treatment strategies. Various kinetic models are available for characterizing adsorption kinetics, with the pseudo-first-order and pseudo-second-order models being commonly employed. To assess the validity of these models, correlation coefficients (R^2) were employed.
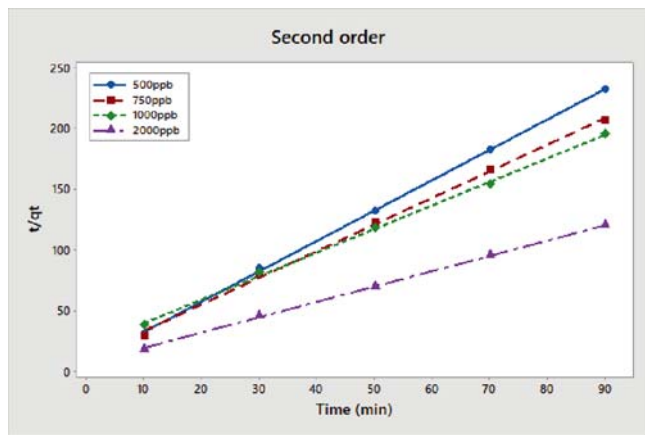

Figure 15. Pseudo-second-order kinetic model

Figures 14 and 15 portray the plots for the pseudo-first-order and pseudo-second-order kinetic models, respectively, illustrating the uptake removal of Hg(II) ions from its aqueous solution by the algal biosorbent. The collected data indicated that the pseudo-second-order model better described the adsorption system compared to the pseudo-first-order model. As outlined in Table 6, the correlation coefficient of the second-order kinetic model surpassed that of the pseudo-first-order model. This concordance underscores that the pseudo-second-order kinetic model effectively characterizes the obtained kinetic data and signifies that the adsorption of Hg by algae follows a natural chemisorption process.

Mass transfer adsorption models

The adsorption mechanism comprises multiple sequential processes, rather than a singular step, encompassing several pivotal stages. Consequently, the uptake of Hg from a solution by algae can be categorized into three distinct phases: (1) the external mass or boundary layer diffusion model, (2) the internal mass diffusion model, and (3) the chemical reaction occurring at the surface. Given that phase 3 is characterized by rapid responsiveness within the adsorption process, phases 1 and 2 assume the role of rate-limiting steps. The contribution of these rate-determining phases, whether they operate individually or collectively, is integral to the progression of the reaction[38, 39].

Weber and Morris model

The Weber and Morris model, rooted in Fick's second law of mass transfer, is commonly employed in the context of the adsorption process to elucidate the mechanism of mass transfer from the exterior surface of the adsorbent to its internal pores[40]. The intraparticle diffusion coefficient, as expressed by Equation 14, is derived through the utilization of the linearized form of the Weber-Morris model equation.

$$q_t = K_{imd}\, t^{0.5} + C \qquad (14)$$

where:
q_t = the adsorption capacity at the time
t = time
K_{imd} = Weber and Morris diffusion coefficient
C = boundary layer thickness
by plot qt against $t^{0.5}$ (Fig. 16) calculated all parameters by slop and intercept.

Figure 16 illustrates the presence of three discernible adsorption phases, substantiating the assertion that the binding of Hg to algae is governed by a comprehensive three-stage mechanism across the spectrum of examined Hg concentrations. In the initial stage (section 1 in Fig. 16), spanning up to 5.5 in x-axis (time), a linear trajectory is observed across all concentrations, indicating the influence of boundary layer diffusion as Hg molecules adhere to the algae's surface. The subsequent phase (section 2 in Fig. 16), encompassing the interval between 5.5 and 7 $(min)^{0.5}$, manifests a consistent linear alignment with all concentrations, attributable to the diffusion of Hg molecules through pores onto the algae. The last stage (section 3 in Fig. 16) of adsorption from 7 to 10 $(min)^{0.5}$ revealed linear graphs for all concentrations, confirming that the adsorption process had achieved equilibrium and that all active sites of algae were completely saturated with Hg molecules. Table 2 details the computed values of the rate constant (K_{imd}),
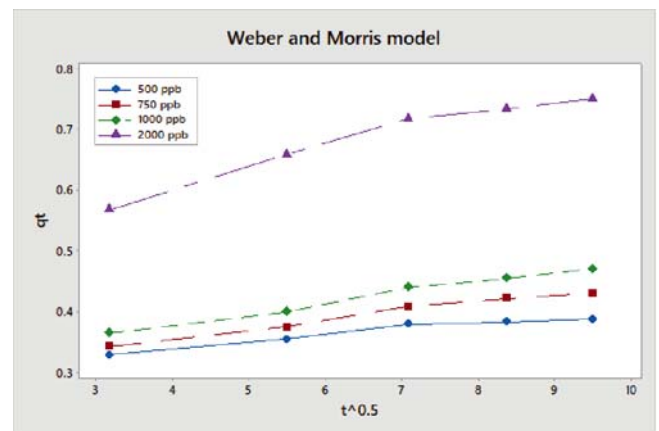

Figure 16. Weber and Morris model

Table 6. Pseudo-first-order kinetic model pseudo-second-order kinetic model

Ci	qe exp	qe cal	K₁	R²	qe cal	K₂	R²
µg/l	µg/g	µg/g	Min⁻¹		µg/g	(g/mg · min)	
500	390	98.8	0.0403	0.984	398	0.9053	0.996
750	440	184.1	0.0382	0.940	454	0.4511	0.998
1000	475	286.4	0.0346	0.982	514	0.1883	0.999
2000	750	353	0.0211	0.976	745	0.2682	0.999

boundary layer thickness (C), and correlation coefficient (R^2) deduced from the linear plots of qt against $(t)^{0.5}$.

As indicated in Table 7, the rate constant (K_{imd}) and boundary layer thickness (C) values exhibited an upward trend with the escalation of Hg content from 500 to 2000 μg/l. The elevation in Hg(II) concentration led to a corresponding increase in the C value, underscoring the significant role played by boundary layer thickness in the adsorption process, thereby influencing the adsorption capacity of algae. Notably, the C values demonstrated an ascent from 301 to 487 μg/g with the augmentation of Hg(II) concentration from 500 to 2000 μg/l, thus highlighting an intensified prevalence of the boundary layer diffusion mechanism under conditions of elevated concentration[41].

Liquid film diffusion model

As per this proposition, a liquid layer composed of adsorbate molecules envelops the surface of the adsorbent. This adsorbate film holds pivotal significance in the adsorption process[39]. In accordance with the Weber--Morris model, both film diffusion and pore diffusion mechanisms could potentially influence the mass transfer dynamics pertaining to the adsorption of Hg onto algae. Through the application of Equation 15, the assessment of diffusion coefficients (K_{fd}) and R^2 values was conducted, and the determined model parameters were compiled in Table 7 with the aid of slope and intercept analysis.
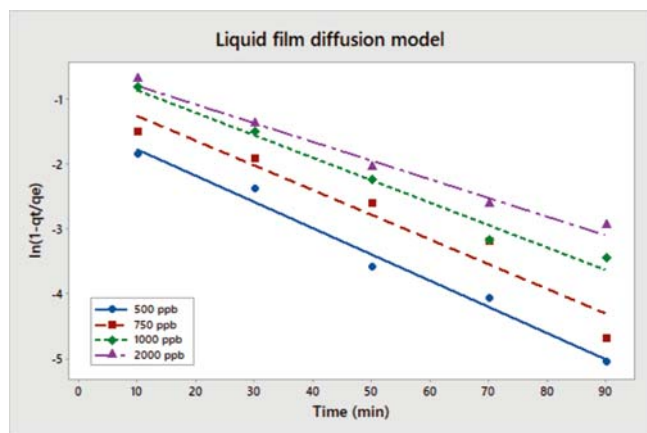
$$\ln(1 - \frac{q_t}{q_e}) = -K_{lf} \qquad (15)$$

Figure 17. Liquid film diffusion model

Where:
q_t = adsorption capacity at time t,
q_e = adsorption capacityat equilibrium, t time
K_{lf} = liquid film diffusion rate constant,
by plot ln(1-qt/qe) against t (Fig. 17) calculated liquid film diffusion rate constant by slope.

This shows that film diffusion is not just a rate-limiting phase in the adsorption of Hg molecules onto algae.

Bangham and Burt model

In specific adsorption systems, pore diffusion exclusively governs the rate-controlling stage. The utilization of the Bangaram and Burt models offers a means to ascertain whether the adsorption process is regulated by pore diffusion or not[42]. Equation 16 presents the linearized expression of the Bangham and Burt model:

$$\log\log(\frac{C_i}{C_i - q_t m}) = \log(\frac{K_b m}{2.303V}) + \alpha_2 \times \log t \qquad (16)$$

Where Ci: is initial concentration, m is th mass of adsorbent, V is the volume of Hg solution, qt is the adsorption capacity at time t, K_b and α_2 are the Bangham's constants, which were calculated by plot $\log\log(\frac{c_i}{c_i - q_t m})$ against log t (Fig. 18) revealed that experimental data did not well fitted with this model. The evidence indicated a strong concordance between the experimental outcomes and this proposed model. The values for the model constant and R^2 are presented in Table 7. Across all concentrations, the R^2 values indicate that the progression of Hg molecule diffusion into the pores
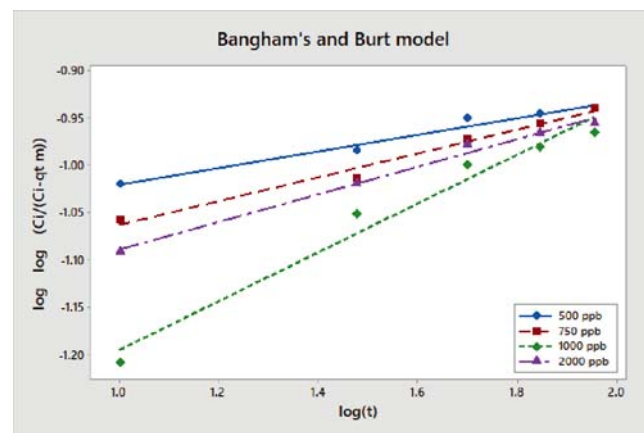

Figure 18. Bangham's and Burt model

Table 7. The values of the rate constant (K_{imd}) and boundary layer thickness (C)

Mass transfer models	Mass transfer model parameter			
Weber and Morris model	Concentration µg/l	K_{imd}	C	R^2
	500	0.0095	0.301	0.9472
	750	0.0151	0.294	0.9914
	1000	0.0317	0.182	0.9453
	2000	0.0293	0.488	0.9547
Liquid film diffusion model	Concentration µg/l	K_{lf}		R^2
	500	0.0403		0.9847
	750	0.0382		0.9914
	1000	0.0346		0.9822
	2000	0.0216		0.9763
Bangham's and Burt model	Concentration µg/l	K_b	α_2	R^2
	500	0.1490	0.088	0.9750
	750	0.0932	0.125	0.9829
	1000	0.0374	0.288	0.9822
	2000	0.0557	0.146	0.9990

of the algae significantly influences the rate, serving as a key controlling factor. Moreover, this diffusion process is influenced by boundary layer diffusion, either in isolation or in conjunction with both layer and pore diffusion mechanisms.

Table 7 illustrates that the rate constant (Kimd) values and boundary layer thickness (C) values exhibited an increase as the concentration of Hg content escalated from 500 to 2000 μg/l.

Comparison Between green algae biomass and another adsorbent

Table 8 compares the adsorption capacities of numerous adsorbents with those of the present study. The tabulated data illustrates that the existing adsorbent exhibits a notably elevated adsorption capacity towards Hg(II) in contrast to alternative adsorbents.

Table 8. Comparison of adsorption capacities for adsorption of Hg(II) ions using various low-cost adsorbents

Adsorbent	Adsorption capacity	References
Cellulose xanthate	600 µg/g	11
Xanthate	1100 µg/g	
Undyed bamboo pulp	9.2 mg/g	43
Undyed sawdust	8.5 mg/g	
Undyed jute	7.6 mg/g	
ACFs-SH	11–14 mg/g	44
POSS-SH	12.9 mg/g	45
Apatite II (TM)	38 mg/g	46
Sulfur-functionalized silica	47.5 mg/g	45
BTESPT-SGs and MPTMS-SGs	93.32 and 102.37 mg/g	47, 48
Algal biomass Coelastrella sp.	750 µg/g	This study

CONCLUSION

In this investigation, the utilization of an environmentally friendly adsorbent, namely green algae, proved effective in the removal of the highly hazardous metal, Mercury, from simulated aqueous solutions. The efficacy of metal ion removal is notably contingent upon the specific adsorption conditions employed. The attainment of equilibrium in the adsorption of Hg(II) ions was achieved within a time frame of 90 minutes, under the conditions of a 40 ^{o}C temperature and a flow rate of 300 ml/min. The applicability of the Langmuir isotherm model and the pseudo-second-order kinetic model was demonstrated in effectively describing the adsorption data for Hg(II), revealing a maximum adsorption capacity of 750 μg/g. This study underscores the considerable potential of green algae biomass as a promising adsorbent for the removal of Hg(II). High removal efficiency encourage researchers to apply green algae to improve wastewater contaminated by heavy metal rather than Hg(II).

ACKNOWLEDGMENTS

LITERATURE CITED

1. Jabbar, N.M., Alardhi, S.M., Al-Jadir, T., & Dhahad, H.A. (2023). Contaminants removal from real refinery wastewater associated with energy generation in microbial fuel cell. *J. Ecol. Eng.* 24(1), 107–114. DOI: 10.12911/22998933/15681.

2. Alardhi, S.M., Ali, N.S., Cata Saady, N.M., Zendehboudi, S., Salih, I.K., Alrubaye, J.M. & Albayati, T.M. (2024). Separation techniques in different configurations of hybrid systems via synergetic adsorption and membrane processes for water treatment: A review, *J. Ind. Engin.Chem.* 130, 91–104. DOI: 10.1016/j.jiec.2023.09.051.

3. Fiyadh, S.S., Alardhi, S.M., Al Omar, M., Aljumaily, M.M., Al Saadi, M.A., Fayaed, S.S., Ahmed, S.N., Salman, A.D., Abdalsalm, A.H., Jabbar, N.M. & El-Shafi, A. (2023). A comprehensive review on modelling the adsorption process for heavy metal removal from waste water using artificial neural network technique, *J. Heliyon.* 9(4). DOI: 10.1016/j.heliyon.2023.e15455.

4. Al-Jadir, T., Alardhi, S.M., Alheety, M.A., Najim, A.A., Salih, I.K., Al-Furaiji, M. & Alsalhy, Q.F. (2022). Fabrication and characterization of polyphenylsulfone/titanium oxide nanocomposite membranes for oily wastewater treatment, *J. Ecol. Eng.* 23(12), 1–13. DOI: 10.12911/22998993/154770.

5. Dawood Salman, A., Alardhi, S.M., AlJaberi, F.Y., Jalhoom, M.G., Le, P.C., Al-Humairi, S.T., Adelikhah, M., Farkas, G. & Abdulhady Jaber, A. (2023). Defining the optimal conditions using FFNNs and NARX neural networks for modelling the extraction of Sc from aqueous solution by Cryptand-2.2.1 and Cryptand-2.1.1, *J. Heliyon.* 9(11). DOI: 10.1016/j.heliyon.2023.e21041.

6. Alardhi, S.M., Aljaberi, F.Y., Kadhim, W.A., Jadir, T.A., Alsaedi, L.M., Jabbar, N. M., Almarmadh, A., Komsh, G.G. & Adnan, M. (2023). Investigating the capability of MCM-41 nanoparticle for COD removal from Iraqi petroleum refinery wastewater, *AIP Conference Proceedings.* 2820(1). DOI: 10.1063/5.0151096

7. Al-Jadir, T., Alardhi, S.M., Al-Sheikh, F., Jaber, A.A., Kadhim, W.A., Rahim, M.H. A. (2023). Modeling of lead (II) ion adsorption on multiwall carbon nanotubes using artificial neural network and Monte Carlo technique. *Chem. Engin. Commun.* 210(10), 1642–1658. DOI: 10.1080/00986445.2022.2129622.

8. Jasim, M.A., AlJaberi, F.Y., Salman, A.D., Alardhi, S.M., Le, P.-C., Kulcsár, G. & Jakab, M. (2023). Studying the effect of reactor design on the electrocoagulation treatment performance of oily wastewater. *Heliyon*, 9(7), e17794. DOI: 10.1016/j.heliyon.2023.e17794.

9. Rio, S. & Delebarre, A. (2003). Removal of mercury in aqueous solution by fluidized bed plant fly ash. *Fuel*, 82(2), 153–159. DOI: 10.1016/S0016-2361(02)00237-5.

10. Gworek, B., Dmuchowski, W., Baczewska, A.H., Brągoszewska, P., Bemowska-Kałabun, O., Wrzosek-Jakubowska, J. (2017). Air contamination by mercury, emissions and transformations—a review. *Water, Air, & Soil Pollution*, 228, 1–31. DOI: 10.1007/s11270-017-3311-y.

11. Hassan, S.S., Awwad, N.S. & Aboterika, A.H. (2008). Removal of mercury (II) from wastewater using camel bone charcoal. *J. Hazard Mater.* 154(1-3), 992–997. DOI: 10.1016/j.jhazmat.2007.11.003.

12. Loureiro, L., Machado, L., Geada, P., Vasconcelos, V., Vicente, A.A. (2023). Evaluation of efficiency of disruption methods for Coelastrella sp. in order to obtain high yields of biochemical compounds release. *Algal Res.* 73, 103158. DOI: 10.1016/j.algal.2023.103158.

13. Liu, H.-Y., Yu, Y., Yu, N.-N., Ding, Y.-F., Chen, J.-M. & Chen, D.-Z. (2022). Airlift two-phase partitioning bioreactor for dichloromethane removal: Silicone rubber stimulated biodegradation and its auto-circulation. *J. Environ. Manag.* 319, 115610. DOI: 10.1016/j.jenvman.2022.115610.

14. Goecke, F., Noda, J., Paliocha, M. & Gislerød, H.R. (2020). Revision of Coelastrella (Scenedesmaceae, Chlorophyta) and first register of this green coccoid microalga for continental Norway. *World J. Microbiol. Biotech.* 36(10), 149. DOI: 10.1007/s11274-020-02897-0.

15. Mtaki, K., Kyewalyanga, M.S. & Mtolera, M.S. (2021). Supplementing wastewater with NPK fertilizer as a cheap so-

urce of nutrients in cultivating live food (Chlorella vulgaris). *Annals Microbiol.* 71(7), 1-13. DOI: 10.1186/s13213-020-01618-0.

16. Alardhi, S.M., Abdalsalam, A.H., Ati, A.A., Abdulkareem, M.H., Ramadhan, A.A., Taki, M.M. & Abbas, Z.Y. (2023). Fabrication of polyaniline/zinc oxide nanocomposites: synthesis, characterization and adsorption of methylene orange. *Polym. Bull.* 81, 1–35. DOI: 10.21203/rs.3.rs-1785804/v2.

17. Alardhi, S.M., Fiyadh, S.S., Salman, A.D. & Adelikhah, M. (2023). Prediction of methyl orange dye (MO) adsorption using activated carbon with an artificial neural network optimization modeling. *Heliyon*, 9(1). DOI: 10.1016/j.heliyon.2023.e12888.

18. Al-Najar, J.A., Al-Humairi, S.T., Lutfee, T., Balakrishnan, D., Veza, I., Soudagar, M. E. M. & Fattah, I.M. (2023). Cost-effective natural adsorbents for remediation of oil-contaminated water. *Water*, 15(6), 1186. DOI:10.3390/w15061186.

19. Remedhan, S.T. (2020). Experimental investigation of thermodynamics, kinetics, and equilibrium of nickel Ion removal from wastewater using zinc oxide nanoparticles as the adsorbent. *Engin. Technol. J.* 38(7), 1047–1061. DOI: 10.30684/etj.v38i7A.60.

20. Yetilmezsoy, K., Demirel, S. & Vanderbei, R.J. (2009). Response surface modeling of Pb (II) removal from aqueous solution by Pistacia vera L.: Box–Behnken experimental design. *J. Hazard Mater*, 171(1-3), 551–562. DOI: 10.1016/j.jhazmat.2009.06.035.

21. Kumar, R., Singh, R., Kumar, N., Bishnoi, K. & Bishnoi, N.R. (2009). Response surface methodology approach for optimization of biosorption process for removal of Cr (VI), Ni (II) and Zn (II) ions by immobilized bacterial biomass sp. Bacillus brevis. *Chem. Engin. J.* 146(3), 401–407. DOI: 10.1016/j.cej.2008.06.020.

22. Singh, K.P., Singh, A.K., Singh, U.V. & Verma, P. (2012). Optimizing removal of ibuprofen from water by magnetic nanocomposite using Box–Behnken design. *Environ. Sci. Pollut. Res.* 19, 724–738. DOI: 10.1007/s11356-011-0611-4.

23. Reddy, D.H.K. & Lee, S-M. (2013). Three-dimensional porous spinel ferrite as an adsorbent for Pb (II) removal from aqueous solutions. *Ind. Eng. Chem. Res*. 52(45), 15789–15800. DOI: 10.1021/ie303359e.

24. Ahmad, R., Kumar, R. & Laskar, M.A. (2013). Adsorptive removal of Pb^{2+} form aqueous solution by macrocyclic calix [4] naphthalene: kinetic, thermodynamic, and isotherm analysis. *Environ. Sci. Pollut. Res.* 20, 219–226. DOI: 10.1007/s11356-012-0838-8.

25. Liu, D., Li, Z., Li, W., Zhong, Z., Xu, J., Ren, J. & Ma, Z. (2013). Adsorption behavior of heavy metal ions from aqueous solution by soy protein hollow microspheres. *Ind. Eng. Chem. Res.* 52(32), 11036–11044. DOI: 10.1021/ie401092f.

26. Wu, D., Zhou, J. & Li, Y. (2009). Effect of the sulfidation process on the mechanical properties of a CoMoP/Al2O3 hydrotreating catalyst. *Chem. Engin. Sci.* 64(2), 198–206. DOI: 10.1016/j.ces.2008.10.014.

27. Almeida, C., Debacher, N., Downs, A., Cottet, L. & Mello, C. (2009). Removal of methylene blue from colored effluents by adsorption on montmorillonite clay. *J. Colloïd Interf. Sci.* 332(1), 46–53. DOI: 10.1016/j.jcis.2008.12.012.

28. Fertu, D.I., Bulgariu, L. & Gavrilescu, M. (2022). Modeling and optimization of heavy metals biosorption by low-cost sorbents using response surface methodology. *Processes*, 10(3), 523. DOI: 10.3390/pr10030523.

29. Igberase, E., Osifo, P. & Ofomaja, A. (2017). The adsorption of Pb, Zn, Cu, Ni, and Cd by modified ligand in a single component aqueous solution: equilibrium, kinetic, thermodynamic, and desorption studies. *Internat. J. Analyt. Chem.* 2017. DOI: 10.1155/2017/6150209.

30. Mohammed, A.A. & Isra'a, S.S. (2018). Bentonite coated with magnetite Fe3O4 nanoparticles as a novel adsorbent for copper (II) ions removal from water/wastewater. *Environ. Technol. & Innovat.* 10, 162–174. DOI: 10.1016/j.eti.2018.02.005.

31. Khan, M.A., Kim, S.-w., Rao, R.A.K., Abou-Shanab, R., Bhatnagar, A., Song, H. & Jeon, B.-H. (2010). Adsorption studies of dichloromethane on some commercially available GACs: effect of kinetics, thermodynamics and competitive ions. *J. Hazard. Mater.* 178(1-3), 963–972. DOI: 10.1016/j.jhazmat.2010.02.032.

32. Azeez, R.A. & Al-Zuhairi, F.K.I. (2022). Biosorption of dye by immobilized yeast cells on the surface of magnetic nanoparticles. *Alexandria Engin. J.*, 61(7), 5213–5222. DOI: 10.1016/j.aej.2021.10.044.

33. Langmuir, I. (1917). The constitution and fundamental properties of solids and liquids. II. Liquids. *J. Amer. Chem. Soc.* 39(9), 1848–1906.

34. Al-Ghouti, M.A. & Da'ana, D.A. (2020). Guidelines for the use and interpretation of adsorption isotherm models: A review. *J. Hazard Mater.* 393, 122383. DOI: 10.1016/j.jhazmat.2020.122383.

35. Wang, J. & Guo, X. (2020). Adsorption isotherm models: Classification, physical meaning, application and solving method. *Chemosphere*, 258, 127279. DOI: 10.1016/j.chemosphere.2020.127279.

36. Dada, A., Olalekan, A., Olatunya, A. & Dada, O. (2012). Langmuir, Freundlich, Temkin and Dubinin–Radushkevich isotherms studies of equilibrium sorption of Zn2+ unto phosphoric acid modified rice husk. *IOSR J. Appl. Chem.* 3(1), 38–45.

37. Arshadi, M., Amiri, M.J. & Mousavi, S. (2014). Kinetic, equilibrium and thermodynamic investigations of Ni (II), Cd (II), Cu (II) and Co (II) adsorption on barley straw ash. *Water Res. Ind. 6*, 1–17. DOI: 10.1016/j.wri.2014.06.001.

38. Sağ, Y. & Aktay, Y. (2000). Mass transfer and equilibrium studies for the sorption of chromium ions onto chitin. *Process Biochem.* 36(1-2), 157–173. DOI: 10.1016/S0032-9592(00)00200-4.

39. Yagub, M.T., Sen, T.K. & Ang, H. (2012). Equilibrium, kinetics, and thermodynamics of methylene blue adsorption by pine tree leaves. *Water, Air, & Soil Pollut.* 223, 5267–5282. DOI: 10.1007/s11270-012-1277-3.

40. Wang, H., Xie, R., Zhang, J. & Zhao, J. (2018). Preparation and characterization of distillers' grain based activated carbon as low cost methylene blue adsorbent: Mass transfer and equilibrium modeling. *Adv. Powder Technol.* 29(1), 27–35. DOI: 10.1016/j.apt.2017.09.027.

41. Yao, S., Zhang, J., Shen, D., Xiao, R., Gu, S., Zhao, M. & Liang, J. (2016). Removal of Pb (II) from water by the activated carbon modified by nitric acid under microwave heating. *J. Colloid Interf. Sci.* 463, 118–127. DOI: 10.1016/j.jcis.2015.10.047.

42. Prajapati, A.K. & Mondal, M.K. (2020). Comprehensive kinetic and mass transfer modeling for methylene blue dye adsorption onto CuO nanoparticles loaded on nanoporous activated carbon prepared from waste coconut shell. *J. Molec. Liquids*, 307, 112949. DOI: 10.1016/j.molliq.2020.112949.

43. Shukla, S. & Skhardande, V. (1992). Column studies on metal ion removal by dyed cellulosic materials. *J. Appl. Pol. Sci.* 44(5), 903–910. DOI: 10.1002/app.1992.070440518.

44. Yao, Y., Velpari, V. & Economy, J. (2014). Design of sulfur treated activated carbon fibers for gas phase elemental mercury removal. *Fuel*, 116, 560–565. DOI: 10.1016/j.fuel.2013.08.063.

45. Arsuaga, J.M., Aguado, J., Arencibia, A. & López-Gutiérrez, M.S. (2014). Aqueous mercury adsorption in a fixed bed column of thiol functionalized mesoporous silica. *Adsorption*, 20, 311–319. DOI: 10.1007/s10450-013-9586-4.

46. Oliva, J., De Pablo, J., Cortina, J.-L., Cama, J. & Ayora, C. (2011). Removal of cadmium, copper, nickel, cobalt and mercury from water by Apatite II™: Column experiments. *J. Hazard. Mater.* 194, 312–323. DOI: 10.1016/j.jhazmat.2011.07.104.

47. Johari, K., Saman, N. & Mat, H. (2014). Adsorption enhancement of elemental mercury onto sulphur-functionalized silica gel adsorbents. *Environ. Technol.* 35(5), 629–636. DOI: 10.1080/09593330.2013.840321.

48. Johari, K., Saman, N. & Mat, H. (2013). A comparative evaluation of mercury (II) adsorption equilibrium and kinetics onto silica gel and sulfur-functionalised silica gels adsorbents. *Canadian J. Chem. Engin.* 92(6), 1048–1058. DOI: 10.1002/cjce.21949.